Large-Eddy Simulation Modeling of Turbulent Flame Synthesis of Titania Nanoparticles Using a Bivariate Particle Description

Yonduck Sung and Venkat Raman
Dept. of Aerospace Engineering and Engineering Mechanics, The University of Texas at Austin, Austin, TX 78712

Heeseok Koo
Flight Vehicle Research Center, Seoul National University, Seoul, 151–742 South Korea

Maulik Mehta and Rodney O. Fox
Dept. of Chemical and Biological Engineering, Iowa State University, Ames, IA 50011

DOI 10.1002/aic.14279
Published online November 19, 2013 in Wiley Online Library (wileyonlinelibrary.com)

Flame-based synthesis of nanoparticles is an important chemical process used for the manufacturing of metal oxide particles. In this aerosol process, nanoparticle precursors are injected into a high-temperature flame that causes precursor oxidation, nucleation, and subsequent growth of solid particles through a variety of processes. To aid computational design of the aerosol process, a large-eddy simulation (LES) based computational framework is developed here. A flamelet-based model is used to describe both combustion and precursor oxidation. The solid phase nanoparticle evolution is described using a bivariate number density function (NDF) approach. The high-dimensional NDF transport equation is solved using a novel conditional quadrature method of moments (CQMOM) approach. Particle phase processes such as collision-based aggregation, and temperature-induced sintering are included in this description. This LES framework is used to study an experimental methane/air flame that used titanium tetrachloride to generate titania particles. The simulation results show that the evolution process of titania nanoparticles is largely determined by the competition between particle aggregation and sintering at downstream locations in the reactor. It is shown that the bivariate description improves the prediction of particle size characteristics, although the large uncertainty in inflow and operating conditions prevent a full scale validation. © 2013 American Institute of Chemical Engineers *AIChE J*, 60: 459–472, 2014
Keywords: LES, CQMOM, detailed $TiCl_4$ oxidation chemistry, mathematical modeling, combustion, turbulence

Introduction

Flame-based synthesis of nanoparticles, in particular metal oxides such as titania, is an important commercial process.[1,2] In this process, nanoparticle precursors are injected into a pre-existing flame, where gas-phase oxidation of the precursor leads to nucleation and subsequent particle evolution. A variety of multiscale processes including agglomeration, surface growth, and sintering occur in a background of turbulent gas-phase combustion. A comprehensive mathematical description of flame synthesis will significantly aid the design and optimization of the chemical process. The focus of this work is the development of a novel large-eddy simulation (LES) based computational tool that couples detailed models for evolving gas-phase combustion and the nanoparticle population.

Numerical simulations of flame synthesis require models for four different components: (1) the background turbulent flow, (2) gas-phase combustion, (3) gas-phase precursor evolution, and (4) nanoparticle population evolution. Moreover, the interaction of these processes must be successfully described. Due to the inherent complexities of each of these components, developing a comprehensive model has been a formidable challenge. Prior numerical studies have predominantly relied on the use of the Reynolds-averaged Navier Stokes (RANS) formulation for describing the turbulent flow,[3–5] along with a one-step global mechanism for both gas-phase combustion and precursor oxidation. The nanoparticle evolution is described by a population balance equation (PBE), which tracks the evolution of the number density function (NDF) as a function of a fixed number of internal coordinates (e.g., volume and surface area). In the simplest model formulation, a monodisperse population is assumed, in which case transport equations for particle number density, volume, and surface area are evolved.[3,4] Yu et al.[5] used a volume-based univariate NDF description in the RANS-based formulation to simulate titania formation.

While these studies clearly show that computational models are valuable in understanding flame synthesis, the inherent modeling assumptions vastly limit the predictive capability of the computational tools. In the RANS approach, the entire turbulent flow phenomenon including the large-scale stirring that controls both gas-phase combustion and precursor oxidation is explicitly modeled. Consequently, RANS solutions are highly sensitive to the coefficients that

This article was published online on November 19, 2013. Some errors were subsequently identified. This notice is included in the online and print versions to indicate that both have been corrected on November 21, 2013.

Correspondence concerning to this article should be addressed to H. Koo at heeseokkoo@gmail.com.

appear in the underlying models. Akroyd et al.[6] developed a joint-composition probability density function (PDF) based description of particle formation in the context of the RANS methodology. Direct numerical simulations[7] provide the most comprehensive description of the gas-phase turbulent flow, but are computationally prohibitive for practical flows of interest. In the recent past, LES has emerged as an attractive tool that is ideally suited for simulating flames that lie in the so-called flamelet limit.[8–11] In LES, the large-scale mixing process is directly simulated while the small-scale physical processes are modeled. Although combustion and precursor oxidation occur exclusively at the small scales, where molecular mixing precedes chemical reactions, LES captures large-scale mixing accurately and provides better input to the small-scale models. Consequently, combustion models developed in the RANS context have been shown to provide very high predictive accuracy when used in the LES framework.[8,9,11]

The use of global chemical kinetics also limits the predictive capability of the computational tool. Because precursor oxidation is primarily controlled by flame temperature, and global mechanisms are adequate for capturing the heat release, these simplified rates have been commonly used. However, to design novel chemical processes, it is important that the underlying processes are comprehensively described. For instance, high-Reynolds-number flames that could support larger throughput of nanoparticles are also prone to local extinction phenomena. Such nonlinear effects cannot be captured using one-step mechanisms. Kraft and coworkers[12] have developed a detailed chemical mechanism for precursor oxidation, which shows that the different component reactions exhibit a wide range of time scales. Consequently, the nanoparticle yield measured in terms of precursor oxidation efficiency could vary significantly based on the flow configuration. Computational tools should therefore incorporate such detailed chemical mechanisms for the description of the gas-phase kinetics. Recently, Mehta et al.[13] compared the detailed Ti oxidation with the global one-step mechanism in experimental flames. They found that detailed Ti oxidation chemistry is more accurate in predicting the particle evolution profiles when compared to experimental results. Their results also point to the need of exploring detailed mechanism with advanced computational methods to observe the effects of turbulence on the aerosol nucleation process.

The description of the nanoparticle population represents another modeling challenge. The use of univariate or monodisperse population assumptions severely restricts the physical processes that could be incorporated. For instance, use of a volume-based population description does not allow sintering processes to be included. The use of multivariate descriptions, and in particular the use of volume and surface area as internal coordinates, will significantly broaden the scope of nanoparticle modeling. In this regard, Kim et al.[14] used a bivariate population description for silica formation in a laminar flow reactor. Extension of the multivariate description to turbulent flow systems will provide an important step toward predicting particle characteristics.

Recently, Sung et al.[15] and Mehta and coworkers[16] have proposed a LES-based modeling framework for turbulent flame synthesis of nanoparticles. In these studies, detailed chemical kinetic models for both gas-phase combustion and precursor oxidation were used. The use of the LES approach also enables the capture of the turbulent flame dynamics. However, the nanoparticle evolution was modeled using a univariate description that did not allow sintering and other surface processes to be included. In high-temperature flames, modification of surface area through the sintering process becomes critically important.[3] In this work, the LES framework is extended to a multivariate population balance description, along with detailed models for gas-phase kinetics and the turbulent flow processes. The conditional quadrature method of moments (CQMOM)[17] is used to solve the two-dimensional (2-D) PBE along with the LES governing equations. The applicability of this computational tool is demonstrated for a titania synthesis experiment based on a methane-air flame with titanium chloride as the precursor.

Modeling Approach

The focus of this work is the modeling of titania particle synthesis using titanium chloride as the precursor in a methane-air flame. The LES-based modeling framework consists of four components: (1) the gas-phase turbulent flow described using the filtered Navier-Stokes equations, (2) gas-phase kinetics for both fuel combustion and precursor oxidation described using the flamelet approach,[15] (3) nanoparticle nucleation model based on the flamelet description,[15] and (4) the CQMOM-based volume-surface area description of the nanoparticle population. Later, the individual components are described in detail.

LES governing equations

In LES of chemically reactive flows, the flow field is decomposed into resolved and subfilter parts using density-weighted filtering operation called Favre filtering. For an arbitrary variable Q, the filtering operation is defined as

$$\tilde{Q}(\mathbf{y},t)=\frac{1}{\overline{\rho}}\int_{-\infty}^{+\infty}\rho Q(\mathbf{x},t)G(\mathbf{x}-\mathbf{y})d\mathbf{x}, \tag{1}$$

where $\tilde{Q}$ is the Favre-filtered variable, $\overline{\rho}$ is the filtered density field corresponding to the density field ρ. Note that $\tilde{\cdot}$ refers to density-weighted Favre-filtering, while $\bar{\cdot}$ refers to nondensity weighted filtering. G is the filtering kernel that removes high-frequency components from the flow field. The filtering operation is applied to the continuity and momentum equations to produce the filtered governing equations:

$$\frac{\partial\overline{\rho}}{\partial t}+\frac{\partial\overline{\rho}\tilde{u}_j}{\partial x_j}=0 \tag{2}$$

and

$$\frac{\partial\overline{\rho}\tilde{u}_i}{\partial t}+\frac{\partial\overline{\rho}\tilde{u}_i\tilde{u}_j}{\partial x_j}=-\frac{\partial\tilde{p}}{\partial x_i}+\frac{\partial\tilde{\tau}_{ij}}{\partial x_j}+\frac{\partial T_{ij}}{\partial x_j}, \tag{3}$$

where $\tilde{\tau}_{ij}$ is the viscous stress tensor based on the filtered variables and $\tilde{p}$ is the modified filtered pressure, given by

$$\tilde{\tau}_{ij}=\overline{\mu}\left(\frac{\partial\tilde{u}_i}{\partial x_j}+\frac{\partial\tilde{u}_j}{\partial x_i}\right)=2\overline{\mu}\tilde{S}_{ij} \tag{4}$$

with $\tilde{S}_{ij}$ being the strain-rate tensor, and

$$\tilde{p}=\overline{P}+\frac{2}{3}\overline{\mu}\frac{\partial\tilde{u}_k}{\partial x_k}\delta_{ij}. \tag{5}$$

Note that the isotropic part of the strain-rate tensor is combined into the pressure term. T_{ij} is the subfilter stresses and defined as follows:

$$T_{ij} = -\overline{\rho}(\widetilde{u_i u_j} - \tilde{u}_i \tilde{u}_j). \quad (6)$$

This term contains the correlations between the velocity component at the small scales, which has to be explicitly modeled in LES. Here, the Smagorinsky model[18,19] is used to close this term:

$$T_{ij} - \frac{1}{3} T_{kk} \delta_{ij} = 2\mu_t \tilde{S}_{ij}, \quad (7)$$

where μ_t is the turbulent eddy viscosity defined as[19]

$$\mu_t = \overline{\rho} C_s \Delta^2 \mathcal{S} \quad \text{or} \quad \nu_t = \mu_t / \overline{\rho} = C_s \Delta^2 \mathcal{S}, \quad (8)$$

where $\mathcal{S} = \sqrt{\tilde{S}_{ij} \tilde{S}_{ij}}$ is the magnitude of the rate-of-strain tensor and Δ is the characteristic filter size. The coefficient C_s is determined using a dynamic procedure,[20,21] which locally adjusts the coefficient based on the LES solution at each time step.

Detailed gas-phase kinetics

Detailed chemistry mechanisms for both gas-phase combustion[22] and precursor oxidation[12] are available. However, to use these mechanisms in LES, filtered scalar transport equations have to be solved for the species that appear in the mechanisms. The combined combustion/precursor oxidation mechanism[15,16] consists of 76 species and 348 reactions. Because LES is computationally expensive, solving a transport equation for each species will prohibitively increase the cost of the simulations. More importantly, these transport equations contain the filtered chemical source term. As chemical reactions occur exclusively at the small scales, the filtered source term cannot be accurately reproduced using the filtered species values. To overcome these limitations, a conserved-scalar approach based flamelet model[15] is used here. Here, detailed chemical mechanism is included but by using a mapping assumption, the transport equation for the conserved scalar alone is solved in LES.

In the steady laminar-flamelet model, the gas-phase thermochemical composition is represented in terms of a conserved scalar:

$$\phi = \{y_1, y_2, \cdots, y_n, T\} = \mathcal{F}(Z, \chi), \quad (9)$$

where y_i is the species mass fraction for n-species description, T is the temperature, Z is the mixture fraction, and $\chi = 2D(\partial Z/\partial x_i)^2$ is the dissipation rate of mixture fraction with D being the diffusivity of the mixture. $\mathcal{F}$ refers to the flamelet mapping that takes in the input variables to provide the gas-phase composition. This mapping function is obtained by solving a simple nonpremixed flow configuration such as a counter-flow diffusion flame.[23] In LES, the filtered chemical compositions and temperature are required. For this purpose, the mapping function is modified as follows:

$$\tilde{\phi} = \mathcal{G}(\tilde{Z}, \widetilde{Z''^2}, \tilde{\chi}), \quad (10)$$

where $\widetilde{Z''^2}$ is the subfilter variance of mixture fraction, and $\mathcal{G}$ denotes the modified mapping function, which is based on the convolution of $\mathcal{F}$ with a subfilter PDF that is parameterized using the input variables.[24,25] The input variables $(\tilde{Z}, \widetilde{Z''^2}, \tilde{\chi})$ will be solved along with the LES governing equations. The transport equation for the filtered mixture fraction is given by

$$\frac{\partial \overline{\rho} \tilde{Z}}{\partial t} + \frac{\partial \overline{\rho} \tilde{u}_j \tilde{Z}}{\partial x_j} = \frac{\partial}{\partial x_j} \left(\overline{\rho} (\tilde{D} + D_t) \frac{\partial \tilde{Z}}{\partial x_j} \right) \quad (11)$$

where $\tilde{D}$ is the molecular diffusivity corresponding to the gas phase mixture, and D_t is turbulent diffusivity of the mixture fraction that is determined using a similar dynamic procedure[21] used for the turbulent viscosity (Eq. 8). Algebraic models are used to obtain the mixture-fraction variance and dissipation rate:[26,27]

$$\widetilde{Z''^2} = C_V \Delta^2 \left(\frac{\partial \tilde{Z}}{\partial x_j} \frac{\partial \tilde{Z}}{\partial x_j} \right) \quad (12)$$

and

$$\tilde{\chi} = 2(\tilde{D} + D_t) \left(\frac{\partial \tilde{Z}}{\partial x_j} \frac{\partial \tilde{Z}}{\partial x_j} \right), \quad (13)$$

where C_V is a model coefficient that is obtained dynamically[26] and Δ is the filter size. The flamelet-based thermochemical state is precomputed using the FlameMaster code[28] for a one-dimensional (1-D) counter diffusion flame configuration. The boundary conditions used for this 1-D system are based on the inflow conditions of the experimental flame configuration[29] to be simulated here. The precomputed flamelet solutions are stored in a stand-alone look-up table format which is used later for LES computation to determine the filtered thermochemical state as well as the filtered density, molecular viscosity, and molecular diffusivity of the gas mixture.

Although, the flamelet model significantly reduces the computational expense, it is not fully suited for modeling precursor oxidation leading to nucleation. In general, the gas-phase combustion processes are reversible in nature leading to an equilibrium solution. Conversely, particle nucleation irreversibly removes material from the gas phase and adds it to the particle phase. As the flamelet look-up tables are made *a priori*, the information about the local nucleation processes cannot be incorporated into the flamelet computation. In order to overcome this problem, Sung et al.[15] proposed a global transport equation model for nucleation. The flamelet tables are constructed using the full chemical kinetics model for combustion and precursor oxidation. In addition, a separate global transport equation for the precursor mass fraction ($TiCl_4$ in this work) is evolved as follows:

$$\frac{\partial \overline{\rho} \tilde{y}_p}{\partial t} + \frac{\partial \overline{\rho} \tilde{u}_j \tilde{y}_p}{\partial x_j} = \frac{\partial}{\partial x_j} \left(\overline{\rho} (\tilde{D} + D_t) \frac{\partial \tilde{y}_p}{\partial x_j} \right) + \tilde{S}_p. \quad (14)$$

The precursor consumption rate is determined by the source term ($\tilde{S}_p$), which is obtained based on the species compositions in the flamelet look-up table as follows. In order to limit the source term based on the local availability of precursor, the following source term expression is formulated:

$$\tilde{S}_p = -\min \left(\sum_i [Ti]_i W_{TiCl_4} / \Delta t, [TiCl_4] W_{TiCl_4} / \Delta t \right), \quad (15)$$

where $\sum_i [\mathrm{Ti}]_i$ is the concentration of Ti that is obtained by summing up the molar concentrations of all Ti-containing chemical species except $TiCl_4$ precursor in the flamelet database. W_{TiCl_4} is the molecular weight of $TiCl_4$. The precursor concentration ($[TiCl_4]$) is obtained from the transport equation (Eq. 14) using

$$[TiCl_4] = \overline{\rho} \tilde{y}_p / W_{TiCl_4} (\mathrm{mol/m^3}). \quad (16)$$

The nucleation rate is determined in a similar manner to ensure that the titania particle concentration is limited by the $TiCl_4$ concentration, but noting that the nuclei are made of five titania molecules:[16]

$$J=\frac{1}{5}\min\left([\mathrm{TiO}_2]N_{\mathrm{av}}/\Delta t, [\mathrm{TiCl}_4]N_{\mathrm{av}}/\Delta t\right), \tag{17}$$

where N_{av} is the Avogadro constant, and $[TiO_2]$ is the molar concentration of titania from the flamelet database. Δt refers to the LES time step, and appears in these expressions to ensure that the consumption is not greater than the local Ti availability. The earlier expression specifies that the true nucleation rate is bounded by the flamelet-based nucleation rate.

Bivariate modeling of nanoparticle population balance using CQMOM

In terms of end use, important particle characteristics such as adsorption and solubility are heavily dependent on the morphology and structure of the final particles. Although particle size is one of the key parameters to be sought, size alone is not sufficient to describe the complicated particulate morphology and structure. Description of these important characteristics requires additional information such as particle surface area. In the NDF context, this additional information is introduced as a new internal coordinate. For a one-point, one-time distribution, a multivariate density function with N internal coordinates $(\zeta_1, \zeta_2, \ldots \zeta_N)$ is expressed as

$$n=n(\zeta_1, \zeta_2, \ldots \zeta_N; \mathbf{x}, t). \tag{18}$$

In this study, we consider a bivariate NDF $n=n(v,a)$ with particle volume as the first coordinate ($\zeta_1=v$) and particle surface area as the second coordinate ($\zeta_2=a$).

Considering a NDF with the two internal coordinates and nucleation, aggregation, and sintering processes, the PBE becomes

$$\underbrace{\frac{\partial n(v,a)}{\partial t}}_{\text{(Rate change)}}+\underbrace{\nabla\cdot(\mathbf{u}n(v,a))}_{\text{(Convection)}}=\underbrace{\nabla\cdot(\Gamma(v,\Phi)\nabla n(v,a))}_{\text{(Particle diffusion)}}+\underbrace{J(\Phi)f(v_0,a_0,\epsilon_1,\epsilon_2)}_{\text{(Nucelation)}}$$
$$+\underbrace{\int_0^a\int_0^v\beta(v-v',v',a-a',a')n(v-v',a-a')n(v',a')dv'da'}_{\text{(Aggregation-birth)}}-\underbrace{\int_0^\infty\int_0^\infty\beta(v,v',a,a')n(v,a)n(v',a')dv'da'}_{\text{(Aggregation-death)}}+\underbrace{\frac{\partial}{\partial a}(S_a(v,a,\Phi)n(v,a))}_{\text{(Sintering)}}, \tag{19}$$

where the particle diffusivity Γ is modeled as given in Eq. 23 below, which accounts for Knudsen number effect. However, in the LES formulation used here, the subfilter turbulent flux, resulting from the filtered convection term in Eq. 19, will be far more dominant compared to the diffusion process. Consequently, this term is expected to have minimal impact on the evolution of the NDF.

$f(v_0,a_0,\epsilon_1,\epsilon_2)$ is a 2-D uniform distribution function for particle formation that is used to describe the nucleated particle distribution.

$$f(v_0,a_0,\epsilon_1,\epsilon_2)=\frac{v_0^k a_0^l\left((1+\epsilon_1)^{k+1}-(1-\epsilon_1)^{k+1}\right)\left((1+\epsilon_2)^{2(l+1)/3}-(1-\epsilon_2)^{2(l-1)/3}\right)}{2\epsilon_1(k+1)(l+1)\left((1+\epsilon_2)^{2/3}-(1-\epsilon_2)^{2/3}\right)}. \tag{20}$$

$\epsilon_1=0.3$ and $\epsilon_1=0.2$ are used in this study, meaning that particle nuclei with volume $v\in[v_0(1-\epsilon_1), v_0(1+\epsilon_1)]$ and area $a\in[a_0(1-\epsilon_2), a_0(1+\epsilon_2)]$ are formed with equal possibility. Here, a_0 and v_0 are computed based on a nucleated particle diameter of 0.682 nm. J, β, and S_a, are the rates of nucleation, aggregation, and sintering, respectively. In this work, the surface growth terms are not included. This is mainly due to the use of the flamelet-based gas phase chemistry description. The laminar flamelet model, as currently used, cannot account for the population-based surface growth process due to the nonlocality of this interaction. In other words, the particle population cannot be uniquely expressed in terms of mixture fraction and scalar dissipation rate. Each of the source term rate expressions is explained below.

The particle collision kernel β for the bivariate NDF is modeled using Fuchs kernel[30,31] that allows the collision regime to change based on local flow conditions. The kernel itself is given by[30,31]

$$\beta(v,v',a,a')=2\pi(d_c+d_c')(\Gamma+\Gamma')\left[\frac{d_c+d_c'}{d_c+d_c'+2(g^2+g'^2)^{1/2}}+\frac{8(\Gamma+\Gamma')}{(c^2+c'^2)^{1/2}(d_c+d_c')}\right]^{-1}. \tag{21}$$

The different terms appearing in the above equation are prescribed as follows. d_c is the effective collision diameter and modeled as follows to fully consider irregularity of colliding particles:

$$d_c=d_p n_p^{1/d_f},\ d_p=6v/a,\ n_p=a^3/(36\pi v^2), \tag{22}$$

where the fractal dimension d_f is assumed to be 2.5, similar to our previous work.[16] The particle diffusion Γ is defined as

$$\Gamma=\frac{k_bT}{3\mu\pi d_c}\left[\frac{5+4\mathrm{Kn}+6\mathrm{Kn}^2+18\mathrm{Kn}^3}{5-\mathrm{Kn}+(8+\pi)\mathrm{Kn}^2}\right], \tag{23}$$

where k_b is the Boltzmann constant and μ and T are fluid viscosity and temperature, respectively. The particle Knudsen number is evaluated using

$$\mathrm{Kn}=2\lambda_f/d_c. \tag{24}$$

Here, λ_f is the gas mean free path. In Eq. 21, $c=\left(8k_bT/(\pi\rho_p v)\right)^{1/2}$ is the thermal velocity based on particle

volume and density. Also in Eq. 21, g is the averaged distance between two particles given by

$$g=\left[(d_c+l)^3-(d_c^2+l^2)^{3/2}\right]/(3d_c l)-d_c, \qquad l=8\Gamma/(\pi c). \quad (25)$$

Sintering describes the surface transformation that alters an aggregate of primary particles into an aggregate with fewer primary particles by minimization of the surface area.[3] In this study, the point-of-contact (POC) model proposed Johannessen et al.[3,4] is used. As the name implies, the model assumes single contact point among equal-sized spherical primary particles. In this model, the sintering rate is based on the number of contact points, primary particle size, and corresponding characteristic coalescence time. For a particle cluster with two primary particles, the sintering rate is described by a contacting-particle rate expression in the form of S_a = (excessive surface area)/(characteristic time).[3,32] If more than two primary particles are subject to coalescence, the rate is dependent on the number of contact points as well and the rate expression in general can be given as S_a = (number of contact points)×(excessive surface area)/(characteristic time). Based on this argument, the sintering rate is modeled as

$$S_a(v,a,\Phi)=\begin{cases}\dfrac{a-a_s}{\tau_f(d_p^*)} & \text{if } n_p\le 2,\\[2ex] (n_p-1)\left(\dfrac{0.41a_p}{\tau_f(d_p)}\right) & \text{if } n_p>2,\end{cases} \quad (26)$$

where a_s is the surface area of a perfect spherical particle (i.e., minimum surface area for a single round particle with volume v) and $\tau_f(d)$ is the characteristic sintering time of two identical spherical particles with the diameter d. a_p is the surface area of a single primary particle. In the POC model, these quantities are found as[4,13]

$$a_s=(36\pi v^2)^{1/3}, \quad a_p=36\pi v^2/a^2, \quad d_p^*=(3v/\pi)^{1/3} \quad (27)$$

$$\tau_f(d_p)=k_0 d_p^m \frac{T}{T_0}\exp\left(\frac{E_A}{R}\left(\frac{1}{T}-\frac{1}{T_0}\right)\right), \quad (28)$$

where $k_0=1\times10^{28}(\mathrm{m}^{-4})$ is a pre-exponential term at $T_0=1400$ (K) and $m=4$ is an exponential power for two identical contacting particles with size d_p. $E_A=1.5\times10^5(\mathrm{J/mol})$ is the activation energy[33] and R is the gas constant. The characteristic sintering time (Eq. 28) is strongly dependent on temperature as well as the sizes of primary particles. As shown in Figure 1, for $T>500$ K, the sintering time increases approximately by order of 10^3-10^5 when the particle size increases only by an order of magnitude. Hence, the sintering process is highly sensitive to the history of gas phase temperature that a particle aggregate encounters in a turbulent flame.

The bivariate NDF involves a six-dimensional transport equation Eq. 19 and is not directly amenable for finite-volume/finite-difference based discretization. In the univariate case, the quadrature method of moments (QMOM) approach[34] is often used. Here, a set of moments of the NDF transport equation are solved. By representing the NDF in terms of a finite number of dirac delta functions, the moments solution are used to reconstruct the NDF. However, this method is not directly applicable as the product-difference algorithm used to obtain the weights and abscissas is not extendible to multivariate NDFs. To overcome this challenge, we use CQMOM proposed in.[35] CQMOM is similar to QMOM in that it utilizes quadrature-approximated delta

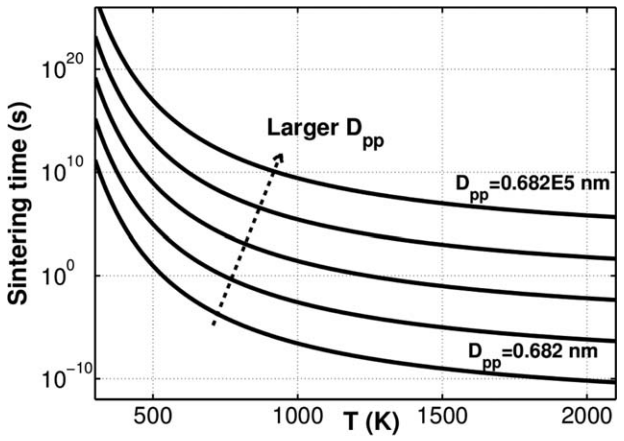

Figure 1. Effect of primary particle size on characteristic sintering time.

functions to model the NDF and uses the production-difference algorithm to recover the weights and abscissas information from selected NDF moments. The main idea of CQMOM is to add a new internal coordinate, being conditioned on a pre-existing internal coordinate. In the bivariate case, the second coordinate a is conditioned on the first coordinate v. From this, NDF in CQMOM can be represented as

$$n(v,a;\mathbf{x},\mathrm{t})=n_V(v)n_{A/V}(a|v)=\sum_{i=1}^{N_v}\sum_{j=1}^{N_a} w_i w_{ij}\delta(v-v_i)\delta(a-a_{ij}), \quad (29)$$

where N_v and N_a are the number of nodes in volume and area directions, respectively. w_i and v_i are the weight and abscissa in the first internal coordinate (volume) and w_{ij} and a_{ij} are the weight and abscissa of the second internal coordinate (area), respectively. The first subscript i in w_{ij} and a_{ij} indicates the j-th node of the second coordinate is conditioned on the i-th node on the first coordinate. As in QMOM, these weights and abscissas are determined using a select set of NDF moments. In CQMOM, the general NDF moment m_{kl} with the k-th order in volume and the l-th order in area is defined as

$$m_{kl}\equiv\int_0^\infty\int_0^\infty v^k a^l n(v,a)dvda=\sum_{i=1}^{N_v}\sum_{j=1}^{N_a} w_i w_{ij} v_i^k a_{ij}^l. \quad (30)$$

The NDF moments are obtained by solving the moment transport equations. The filtered CQMOM moment transport equations are found in a similar manner to that used for the univariate QMOM moment transport equation.[15] First, we obtain the filtered transport equation for n by applying the filtering operation.[15] Similar to the QMOM case, this procedure yields several unclosed terms:

$$\frac{\partial\overline{n}}{\partial t}+\nabla\cdot(\overline{\mathbf{u}}\overline{n})=\nabla\cdot(\overline{\Gamma\nabla n})-\nabla\cdot(\overline{\mathbf{u}n}-\overline{\mathbf{u}}\overline{n})+\overline{J}_{kl}f(v_0,a_0,\epsilon_1,\epsilon_2)$$
$$+\int_0^a\int_0^v\overline{\beta(v-v',v',a-a',a')n(v-v',a-a')n(v',a')}dv'da'$$
$$-\int_0^\infty\int_0^\infty\overline{\beta(v,v',a,a')n(v,a)n(v',a')}dv'da'+\frac{\partial\overline{S_a n}}{\partial a}. \quad (31)$$

The unclosed terms are modeled similar to the QMOM case.[15] For example, identical closures used in Sung et al.[15]

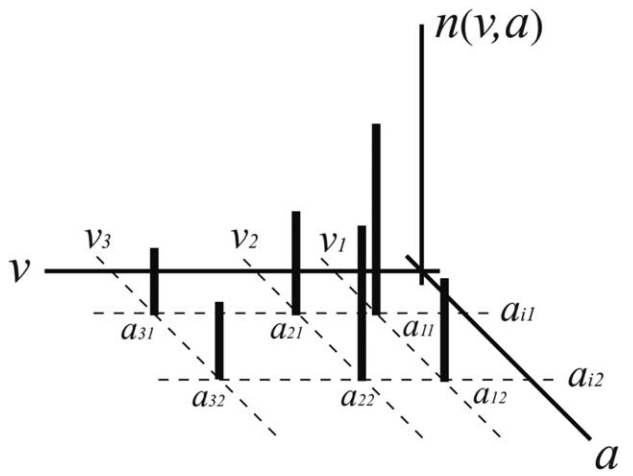

Figure 2. An example of a CQMOM-approximated bivariate particle size distribution $n(v,a)$ using three volume nodes ($N_v=3$) and two conditional area nodes ($N_a=2$).

are used to close the subfilter NDF flux term and particle diffusion term. Then the filtered moment transport equation for m_{kl} is found by integrating the NDF equation over volume and surface area dimensions as

$$\int\int v^k a^l \times (\text{Eq. } 31)\, dv da \tag{32}$$

by assuming negligible correlations and laminar closure. The resulting filtered LES transport equation can be written as follows:

$$\begin{aligned}\frac{\partial \overline{m}_{kl}}{\partial t}+\nabla\cdot(\tilde{\mathbf{u}}\overline{m}_{kl}) &= \nabla\cdot((\overline{\Gamma}+D_t)\nabla\overline{m}_{kl}) \\ &\quad +\overline{J}_{kl}+\overline{B}_{kl}-\overline{D}_{kl}-\overline{S}_{a,kl},\end{aligned} \tag{33}$$

where

$$\begin{aligned}\overline{J}_{kl} &= \overline{J}\,\frac{v_0^k a_0^l((1+\epsilon_1)^{k+1}-(1-\epsilon_1)^{k+1})((1+\epsilon_2)^{2(l+1)/3}-(1-\epsilon_2)^{2(l-1)/3})}{2\epsilon_1(k+1)(l+1)((1+\epsilon_2)^{2/3}-(1-\epsilon_2)^{2/3})},\\
\overline{B}_{kl} &= \frac{1}{2}\sum_{i=1}^{N_v}\sum_{j=1}^{N_a}\sum_{m=1}^{N_v}\sum_{n=1}^{N_a}\beta(\overline{v}_i,\overline{a}_{ij},\overline{v}_m,\overline{a}_{mn})\overline{w}_i\overline{w}_{ij}\overline{w}_m\overline{w}_{mn}(\overline{v}_i+\overline{v}_m)^k(\overline{a}_{ij}+\overline{a}_{mn})^l,\\
\overline{D}_{kl} &= \frac{1}{2}\sum_{i=1}^{N_v}\sum_{j=1}^{N_a}\sum_{m=1}^{N_v}\sum_{n=1}^{N_a}\beta(\overline{v}_i,\overline{a}_{ij},\overline{v}_m,\overline{a}_{mn})\overline{w}_i\overline{w}_{ij}\overline{w}_m\overline{w}_{mn}(\overline{v}_i^k\overline{a}_{ij}^l+\overline{v}_m^k\overline{a}_{mn}^l),\\
\overline{S}_{a,kl} &= \sum_{i=1}^{N_v}\sum_{j=1}^{N_a} l\overline{w}_i\overline{w}_{ij}\overline{v}_i^k\overline{a}_{ij}^{l-1}\overline{S}_a.\end{aligned} \tag{34}$$

As in QMOM, the source terms are closed using a laminar chemistry assumption. Again, it is important to note that the "filtered" weights and abscissas in the above equations ($\overline{w}$, $\overline{v}$, and $\overline{a}$) are computed from the filtered moments and therefore they are not equivalent to the actual filtered weight and abscissa. With the moment information known from Eq. 33, the weights and abscissas are found by using the following steps.[35] The filtering notation is removed for brevity.

1. First, find the volume node weights and abscissas ($w_1,\ldots,w_{N_v}$ and $v_1,\ldots,v_{N_v}$) from $2N_v$ number of the pure volume moments ($m_{00},m_{10},\ldots,m_{2(N_v-1),0}$) via the product-difference algorithm. This procedure is identical to that of the univariate QMOM case[15]).
2. Once the volume nodes are found, the conditional area node information can be determined by following the substeps listed below
   a. Using the CQMOM definition of m_{kl}

$$m_{kl}=\sum_{i=1}^{N_v}\sum_{j=1}^{N_a} w_i w_{ij} v_i^k a_{ij}^l = \sum_{i=1}^{N_v} w_i v_i^k A_{il}, \tag{35}$$

   construct a linear equation system for $A_{il}=\sum_{j=1}^{N_a} w_{ij}a_{ij}^l$, the l-th area moment for the i-th volume node, and solve it for each $l=1,2,\ldots,2N_a-1$. For example, for $l=1$ when $N_v=3$, following linear system is constructed with a Vandermonde matrix:

$$\begin{bmatrix} m_{01}\\ m_{11}\\ m_{21}\end{bmatrix} = \begin{bmatrix} 1 & 1 & 1\\ v_1 & v_2 & v_3\\ v_1^2 & v_2^2 & v_3^2\end{bmatrix}\begin{bmatrix} w_1 & & \\ & w_2 & \\ & & w_3\end{bmatrix}\begin{bmatrix} A_{11}\\ A_{21}\\ A_{31}\end{bmatrix}$$

$$\Rightarrow \begin{bmatrix} A_{11}\\ A_{21}\\ A_{31}\end{bmatrix} = \begin{bmatrix} 1/w_1 & & \\ & 1/w_2 & \\ & & 1/w_3\end{bmatrix}\begin{bmatrix} 1 & 1 & 1\\ v_1 & v_2 & v_3\\ v_1^2 & v_2^2 & v_3^2\end{bmatrix}^{-1}\begin{bmatrix} m_{01}\\ m_{11}\\ m_{21}\end{bmatrix}. \tag{36}$$

   b. At each volume node i, retrieve the conditional weights and abscissas (w_{ij},a_{ij}) from $A_{il}=\sum_{j=1}^{N_a} w_{ij}a_{ij}^l$ using the product-difference algorithm.

From the above procedure, it is clear that the goal of CQMOM is to seek a QMOM-approximated area distribution ($w_{i1},w_{i2},\ldots,w_{ij}$ and $a_{i1},a_{i2},\ldots,a_{ij}$) for each volume node ($w_i,v_i$), which is computed ahead of time by using ordinary QMOM. Consequently, the product-difference algorithm must be applied at each volume node to determine the conditional area nodes. As a result, in CQMOM, the total number of moments required is only $2N_v+N_v(2N_a-1)$, where $2N_v$ is the number of pure volume moments needed to find the volume nodes (w_i,v_i), and $N_v(2N_a-1)$ is the number of pure area and mixed volume-area moments needed to find the conditional area nodes (w_{ij},a_{ij}). An example moment set required for a case with $N_v=N_a=3$ is presented in Table 1. Compared to the univariate case, the cost of bivariate expansion is equal to $N_v(2N_a-1)$ additional equations, which does not impose a large cost since scalar transport equations are relatively inexpensive compared to momentum equations. Besides, CQMOM takes advantage of QMOM routines such as the product-difference algorithm and requires no additional modifications for the bivariate case. In other words, CQMOM offers a very attractive approach for a low-cost expansion to bivariate NDF modeling as compared to the univariate QMOM.

In this study, three volume nodes ($N_v=3$) and one conditional area node ($N_a=1$) is used. This particular setup requires a total of nine NDF moments, six for the pure volume moments ($m_{00},m_{10},\ldots,m_{50}$, which are the same for the single variable QMOM case), and three for the area or volume-area mixed moments (m_{01},m_{11},m_{21}). Compared to QMOM, only three additional equations are solved and hence the computational cost increase is rather mild for the accrued benefits of bivariate modeling.

Table 1. An Example of the Required List of CQMOM Moments for Bivariate NDF Modeling with $N_v = N_a = 3$[35]

m_{00}	m_{01}	m_{02}	m_{03}	m_{04}	m_{05}	
m_{10}	m_{11}	m_{12}	m_{13}	m_{14}	m_{15}	
m_{20}	m_{21}	m_{22}	m_{23}	m_{24}	m_{25}	
m_{30}	↓	↓	↓	↓	↓	
m_{40}	A_{11}	A_{12}	A_{13}	A_{14}	A_{15}	$\rightarrow \{w_{1j}, a_{1j}\}$
m_{50}	A_{21}	A_{22}	A_{23}	A_{24}	A_{25}	$\rightarrow \{w_{2j}, a_{2j}\}$
↓	A_{31}	A_{32}	A_{33}	A_{34}	A_{35}	$\rightarrow \{w_{3j}, a_{3j}\}$
$\{w_i, a_i\}$						

It is noted that although the PBE is filtered without using density-weighting, the equation could be recast in terms of density-weighted filtering (which will be similar in form to scalar transport equations such as the precursor equation, Eq. 14). In the numerical implementation, only the Favre-filtering form is used.

Addition of the sintering process poses a numerical difficulty mainly due to the high sensitivity of the sintering rate expression (Eq. 26) to the gas-phase conditions, especially temperature. Numerically, this sensitivity increases the stiffness of the ODE solver, causing the solver to sometimes fail due to the exceedingly small inner time-step used. Here, this technical difficulty has been overcome by utilizing a new operator-split ODE integration method (Mehta et al., submitted). The basic idea behind this method is that the CQMOM weights are not affected by surface reactions, or sintering process (Eq. 26). In other words, only changes in surface area or volume occur during these processes. In this method, the ODE integration is divided into two parts. The first part of the ODE handles the nucleation and aggregation events, including the weights of the CQMOM discretization:

$$\overline{m^{(1)^*}}_{kl}^{\,t+\Delta t} = \int_0^{\Delta t} \left(\overline{J}_{kl} + \overline{B}_{kl} - \overline{D}_{kl}\right) dt, \tag{37}$$

where Δt denotes LES time step and $m^{(1)^*}$ denotes the interim moment solutions for the first part of the ODE split process. After the first integration, the weights (w_i^* and w_{ij}^*) are found using the product-difference algorithm.[36] These weights are then fixed in time for the second part of the ODE integration.

In the second part, the sintering processes are considered. During this process, only the area abscissas change, and therefore, the second ODE integration is carried out in terms of the abscissas instead of the moments. Now sintering leads to changes in only the area abscissas (a_{ij}), hence, an equation to account for this change can be written as

$$\overline{a_{ij}^*}^{\,t+\Delta t} = -\int_0^{\Delta t} \overline{S}_a(v_i, a_{ij}, \Phi) dt. \tag{38}$$

The new solution of the abscissas then, together with the weights (w_i and w_{ij}) found from the moments after the first ODE integration, are used to find the updated final moment set:

$$\overline{m^{(2)^*}}_{kl} = \sum_{i=1}^{N_v} \sum_{j=1}^{N_a} w_i w_{ij} (v_i)^k (a_{ij}^*)^l. \tag{39}$$

The final source term for Eq. 33 is then determined as follows:

$$S_{kl}^{\text{total}} = \frac{\overline{m^{(2)^*}}_{kl} - \overline{m}_{kl}}{\Delta t}, \tag{40}$$

where S_{kl}^{total} is the sum of the all sources for m_{kl} in Eq. 33.

Simulation of a Titania Flame-Synthesis Experiment

The LES-CQMOM approach detailed in the previous section is applied to an experimental burner used for generating titania particles. Figure 3 provides a schematic representation of the different solvers involved in the LES framework. Below, details of the simulation configuration, the computational details, and the results are discussed.

Flame configuration

The CQMOM-LES model is demonstrated using the Flame D configuration in Pratsinis et al.[29] for two different air flow rates of 3800 mL/min and 5500 mL/min. The reactor geometry as well as the flame configuration are shown in Figure 4. The reactor consists of three concentric passages with a main center nozzle and two annuli. The inner diameter of the center nozzle is 4 mm while the width of two concentric annuli are 1 mm each. The wall thickness is 1 mm for all the inflow nozzles. A mixture of CH_4, prevaporized $TiCl_4$, and argon issues from the main jet and air issues from the outer annulus. From the inner annulus, only minimal amount of air is issued just enough to prevent particle deposit in or near the passage. In the simulations, this is enforced by flowing a small amount of air, which is 3% mass of the air flow rate from the outer annulus. Since the fuel and oxidizer are separated at the inlet, the flame operates in the nonpremixed combustion regime. The mixture fraction is set to one for the fuel inlet and zero for all other inlets. The flow rates of the different streams used in the simulations are presented in Table 2.

Simulation setup and numerical methods

A low-Mach number, variable density LES formulation is used here.[37] The filtered flow equations are solved in the cylindrical coordinate frame, with a domain length of 40D and a radius of 15D, where D is the inner diameter of the central jet. The domain is discretized using 192×96×32 grid cells in the axial, radial, and azimuthal directions, respectively. The momentum equation (Eq. 3) is solved using a second-order, energy conserving scheme,[27] while the scalar equations (Eqs. 11, 14, 33) are solved using a fifth-order weighted essentially nonoscillatory (WENO) scheme.[37,38] CQMOM utilizes precisely the same six QMOM integer volume moments ($m_{00}, \ldots, m_{50}$) used in Sung et al.[15] to describe the NDF with the three volume nodes. Unlike QMOM, however, three additional volume-area mixed moments (m_{01}, m_{11}, m_{21}) are solved in order to recover conditional

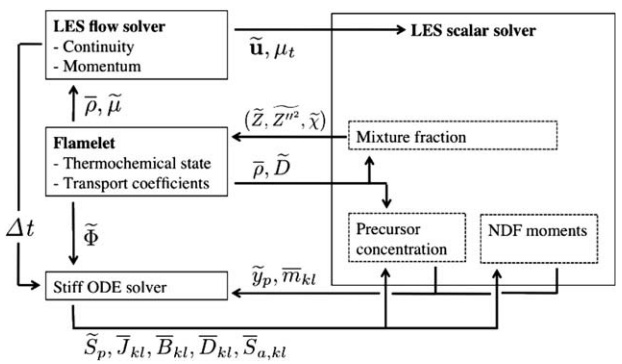

Figure 3. A diagram showing the structure of the LES-based computational solver.

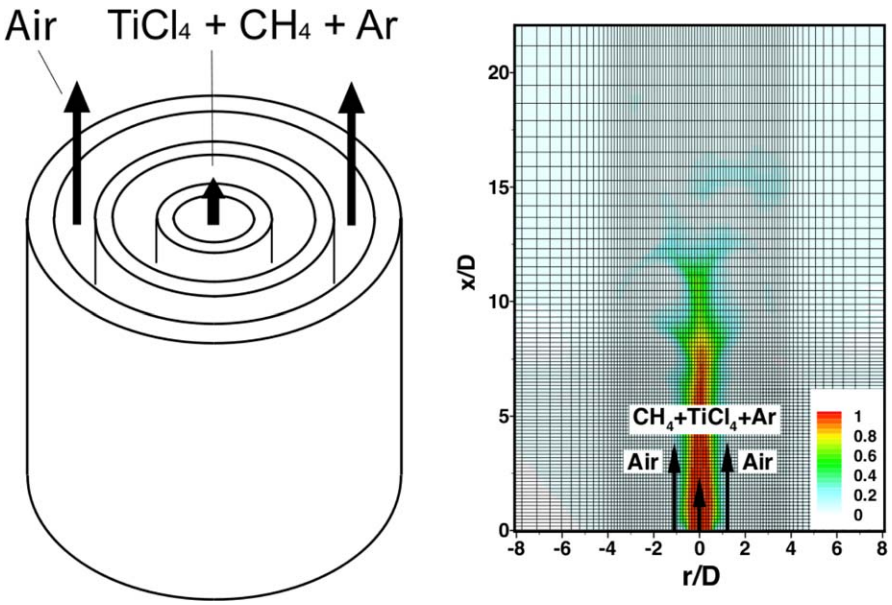

Figure 4. A schematic of the flame configuration used (left) and part of the grid system used (right) for the LES computations.

Denotes the inner diameter of center jet (4 mm) and all walls are 1-mm thick. The background contour shown in the left figure is the mixture fraction variable, which is defined to be 1 at the exit of the center nozzle and zero otherwise. Note that only 1 out of 3 computational grid cells are shown for the sake of clarity. [Color figure can be viewed in the online issue, which is available at wileyonlinelibrary.com.]

area node information. The simulations were carried out using MPI-based domain decomposition on 128–256 processors. Statistical averages were computed after the flow reaches stationarity. With 128 processors, the total computational time is roughly 6 days for each case. This corresponded to 30 residence times based on the center-jet inflow velocity and the length of the domain. The statistical averages were collected over the last seven residence times. Additional tests using sampling windows were used to ensure that the statistics have converged.

Results and Discussion

Flame characteristics

The cases studied here correspond to canonical nonpremixed flames. This is clearly seen in the instantaneous plots of temperature (Fig. 5) for the two cases. Case B is based on a lower flow rate of oxidizer, which corresponds to a lower velocity for the air stream. Consequently, the fuel jet undergoes less shear-induced breakdown and exhibits a longer core region. In both cases, the high temperature zone corresponding to the flame front is located primarily near the stoichiometric fuel composition (denoted by the dashed lines in Fig. 5). At the end of the jet core, intense fuel-air mixing leads to a closed flame. The flame length, defined by the jet core length, is significantly different for the two cases, with the lower air velocity leading to longer flames. Figure 5 also shows the time-averaged temperature profiles for the two cases. Although the air flow velocity changes the shape and size of the high temperature region, the average temperature in post jet-core region appears to be nearly the same for the two cases.

The axial and radial profiles of the time-averaged temperature are further shown in Figures 6 and 7, respectively. The time-averaged centerline temperatures (Fig. 6) indicate that the fuel jet breakdown occurs at approximately $x/D = 6$ for case A and $x/D = 8$ for case B. The increase in temperature is due to the intense mixing at the edge of the jet core as seen in the 2-D plots (Fig. 5). The radial profiles (Fig. 7) show that the peak in temperature occurs in a narrow zone at the interface of the fuel and air streams, which expands through entrainment and turbulent diffusion as the jet moves downstream. Further, it should be noted that the centerline temperature, even for case B, reaches a value of approximately 500 K by $x/D = 9$. This aspect is important for understanding the nucleation process (discussed below). The values and locations of the maximum centerline temperature of the flame are marked in Figure 6. The LES computations underpredict the maximum temperatures and the locations of the peak temperature. However, it is seen that both flames break down essentially at similar lengths. The difference with experiments suggests that in the experiments the flames breakdown slower, indicating a reduced turbulence intensity in the jet at exit. It is known that minor variations in the inflow mean velocity profile or turbulence intensity could significantly alter the quantitative features of the flame in any LES computation.[10] Note that the LES computations still predict the qualitative trends in terms of flame length correctly.

Nanoparticle evolution

The first step toward nanoparticle creation is the oxidation of the titanium tetrachloride precursor. This multistep

Table 2. Flow Rates Used for LES Computation

	Case A	Case B
CH_4	312 mL/min	312 mL/min
$TiCl_4$	5.8×10^{-4}mol/min	5.8×10^{-4}mol/min
Ar	250 mL/min	250 mL/min
Air	5500 mL/min	3800 mL/min

The flame configuration is corresponding to Flame D setup in Pratsinis et al.[29]

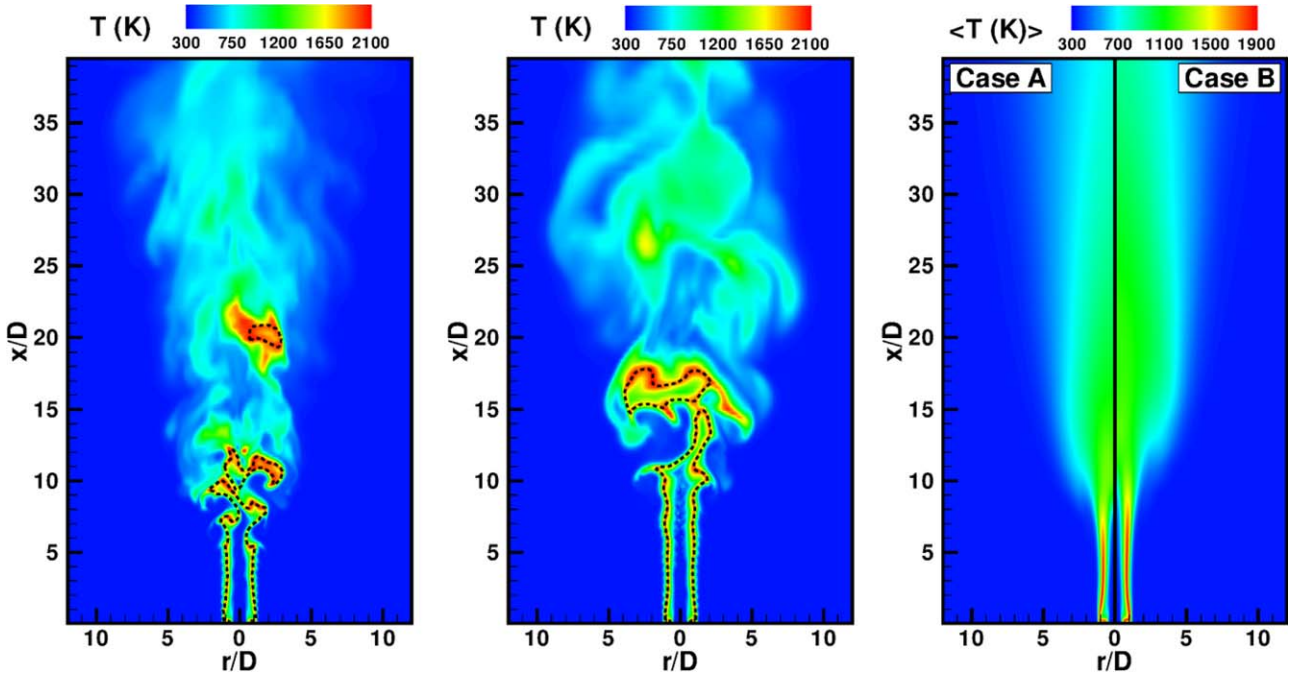

Figure 5. Instantaneous contour plots of the temperature fields for (left) case A, (center) case B, and the mean temperatures for both cases (right).

The dotted lines indicate the stoichiometric mixture composition. [Color figure can be viewed in the online issue, which is available at wileyonlinelibrary.com.]

process, described here using a detailed chemical kinetic mechanism,[12] is highly temperature sensitive. Figure 8 shows the instantaneous precursor concentration for the two cases studied here, along with the stoichiometric surface (dashed lines). It is seen that precursor oxidation occurs away from the stoichiometric surface, in the fuel-rich part of the jet. Note that temperatures higher than 400 K lead to significant nucleation. In both cases, the precursor is consumed long before the jet core breaks down. Figure 9 shows the time averaged number density (m_{00}) fields from the two cases. It is seen that the highest number density occurs at the outer edge of the high-concentration precursor zone (Fig. 8) and is not significantly different quantitatively for both cases. The particle number density is highest only in these regions in the entire domain. This indicates that nucleation is confined to the rich mixture by the flamelet-based oxidation model, and that other processes such as agglomeration become active subsequently to reduce the number density.

The evolution of the nanoparticles is controlled by nucleation, agglomeration, and sintering. The collision-based aggregation model depends on the square of the number density ($\overline{B}_{kl}$ and $\overline{D}_{kl}$ in Eq. 34), and is most active in regions of high number density. Therefore, intensive aggregation is observed very close to the nucleation region (Fig. 9), where elevated temperatures further accelerate the collision process. As a result, particle aggregates with large surface area and relatively small volume are formed from the small nucleated particles. Figure 10 shows plots of the instantaneous conditional area abscissas for case A. High surface area is prominent near the burner exit where nucleated particles are aggregated in the high temperature zone. The surface area decreases as the flow moves downstream due to sintering effect. Figure 11 presents the volume abscissas plots corresponding to Figure 10. It is noted that particles with small volumes are formed in the near field where the particle surface area is high. The particle volume abscissas then stay relatively uniform further downstream. This behavior indicates that nucleation followed by aggregation is the main mechanism behind particle evolution in the near-field of the flame configuration. The abscissa behaviors are summed up in Figure 12, which shows time-averaged area and volume abscissa profiles as well as number density of each abscissa node along the centerline. The first abscissa node, which represents the smallest size, is associated with the largest weight or number density, indicating that this abscissa is dominant in determining the evolution of the nanoparticles. Similar behavior is observed for case B and is not shown here.

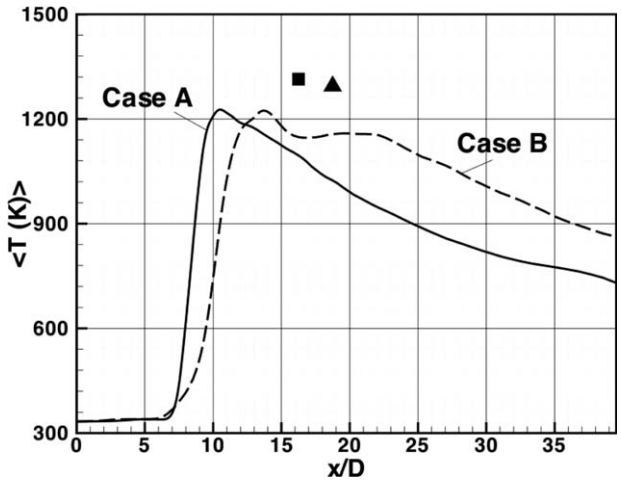

Figure 6. Mean temperature profiles along the center line.

Peak temperature values and locations measured in the experiment[29] are marked as a square symbol (case A) and a triangle (case B).

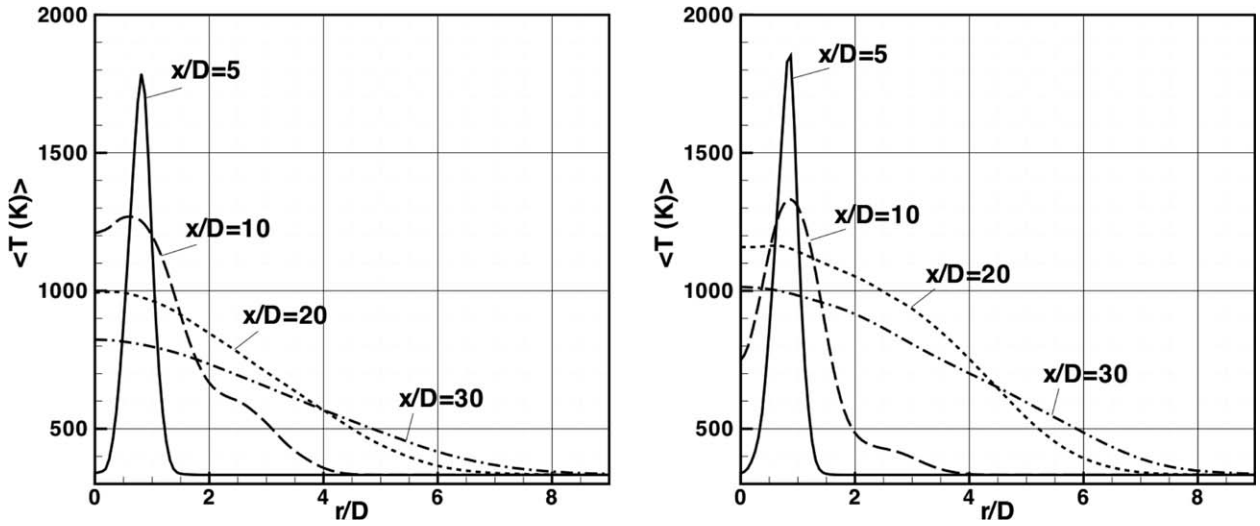

Figure 7. Mean temperature profiles in radial direction for (left) case A and case B (right) at select axial locations.

Since both particle volume and surface area information is available from the CQMOM representation, the particle aggregate structure can be studied. Using the number density (m_{00}), the average particle volume (m_{10}/m_{00}) and surface area (m_{01}/m_{00}) is calculated. Here m_{10} and m_{01} are the total particle volume and surface area in a unit volume of gas, respectively. m_{10} and m_{01} can also be used to find the average primary particle size[13]

$$D_{pp} = \frac{6m_{10}}{m_{01}}. \tag{41}$$

Based on the average primary size, we can also find out the number of primary particles in the aggregates by assuming that the average particle volume consists of the sum of N_{pp} primary particles with diameter D_{pp}. The resulting expression is given by

$$N_{pp} = \frac{m_{01}^3}{36\pi m_{00} m_{10}^2}. \tag{42}$$

Figure 13 shows the instantaneous fields and time-averaged centerline profiles of the size and number of primary nanoparticles for case A. The number of primary particles are highest close to the edge of the jet core, where nucleation rates are high and the temperature is elevated. This result is consistent with the conditional area abscissas shown in Figure 10. Due to intense aggregation, a large number of small primary particles are contained in the aggregates. As these aggregates move downstream, sintering increases the size of the primary particles. It is also seen that the size of the primary particles does not change significantly past the jet breakdown region, which is primarily due to reduction in sintering rates at lower temperatures (see Fig. 1).

In the time-averaged centerline profiles (Fig. 13), it is seen very clearly that aggregation initially increases the

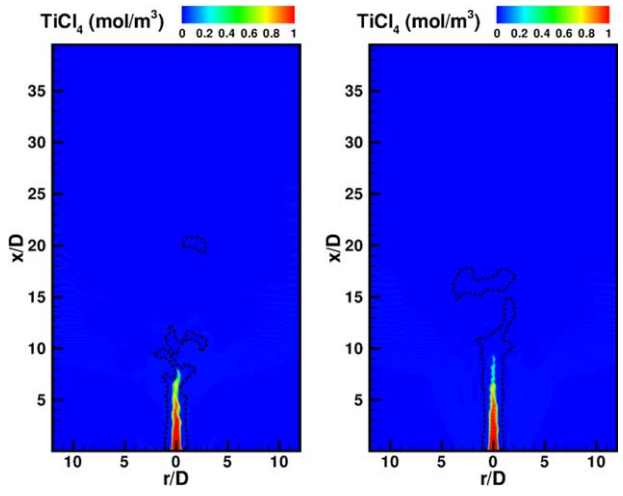

Figure 8. Instantaneous contour plots of the precursor concentration for (left) case A and (right) case B.

The dashed lines indicate stoichiometric mixture composition. [Color figure can be viewed in the online issue, which is available at wileyonlinelibrary.com.]

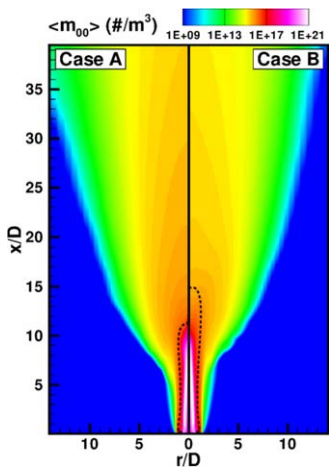

Figure 9. Mean contour plots of the particle number density m_{00}.

The dashed lines indicate stoichiometric mixture composition. [Color figure can be viewed in the online issue, which is available at wileyonlinelibrary.com.]

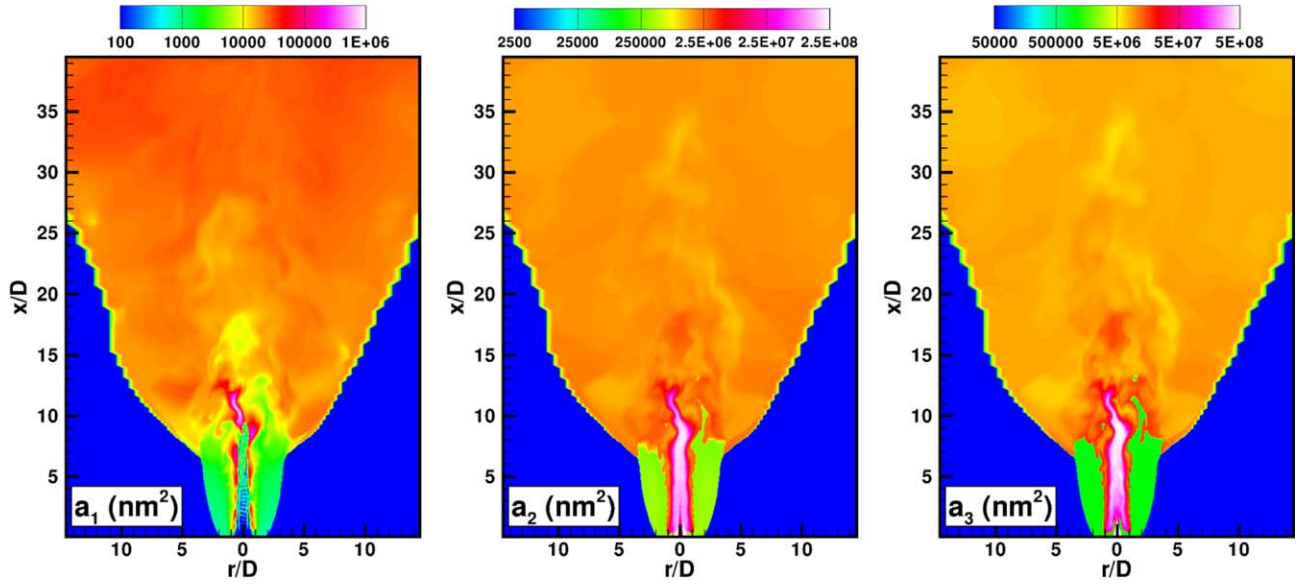

Figure 10. Instantaneous contour plots of the conditional area abscissas for case A.

[Color figure can be viewed in the online issue, which is available at wileyonlinelibrary.com.]

number of primary particles, but the high temperature region leads to a sintering-dominated increase in primary particle size. Here, the number of primary particles decreases. Further downstream, where sintering is less important due to reduced gas phase temperatures, it is found that aggregation is slightly higher than sintering itself leading to a slow increase of the number of primary particles. Figure 14 compares the magnitude of aggregation and sintering sources acting on the lowest-order moments, which are number density (m_{00}) and area (m_{01}) moment, respectively. The sources are divided by the associated moments to compare relative importance. It is seen that both sources decrease drastically past the main flame region, but the sintering rates drop faster than the aggregation rate. This is mainly due to the fact the particles are nearly spherical at this point in spite of large primary particle sizes. Note that both source terms plotted in Figure 14 work as sinks that lower the particular moments, although volume and conditional area abscissas increase from the aggregation process.

Using the CQMOM information, the increase in particle size is studied using the ratio of LES-filter scale volume concentration and the monomer volume (v_0) or area concentration and the monomer surface area (a_0), normalized by the number density. The time-averaged profiles of this quantity are shown in Figure 15 for the two cases. This quantity provides a measure of the growth of the nanoparticle volume. Without surface growth and using constant fractal dimension, the increase in volume is solely driven by aggregation. The time-averaged profiles show significant growth in the near-field for the faster air-stream case (case A), while the particles of the slower air-stream case eventually grow into larger area and volume than those of the faster jet. Due to longer flame in case B, particles reside longer in the colder area where aggregation occurs more and particles could

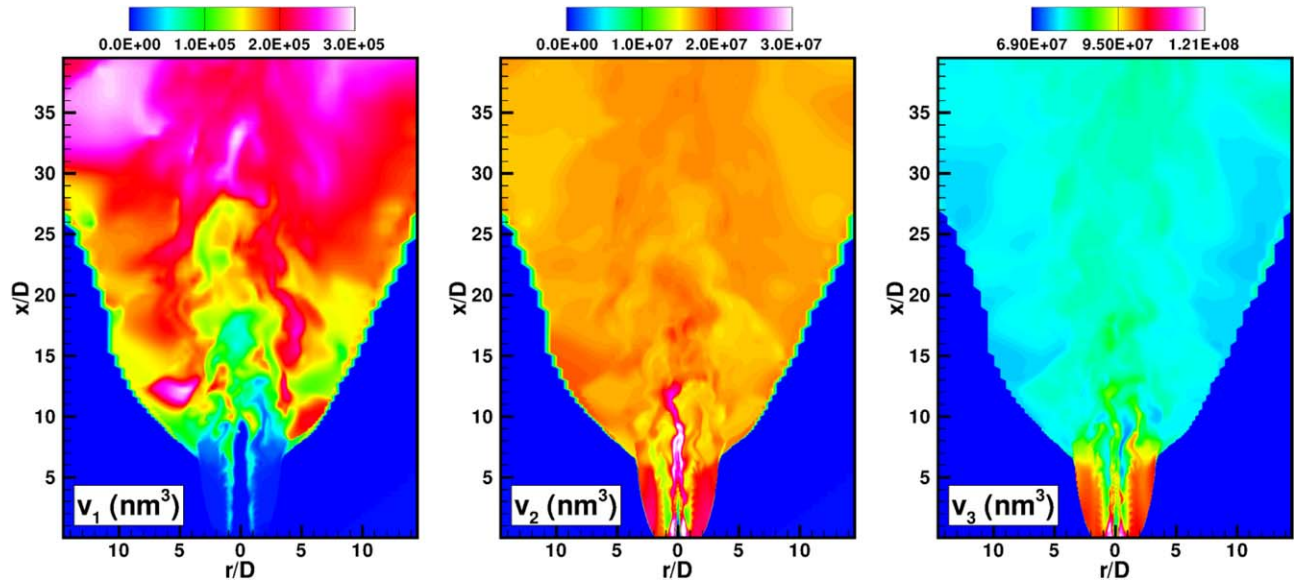

Figure 11. Instantaneous contour plots of the volume abscissas for case A.

[Color figure can be viewed in the online issue, which is available at wileyonlinelibrary.com.]

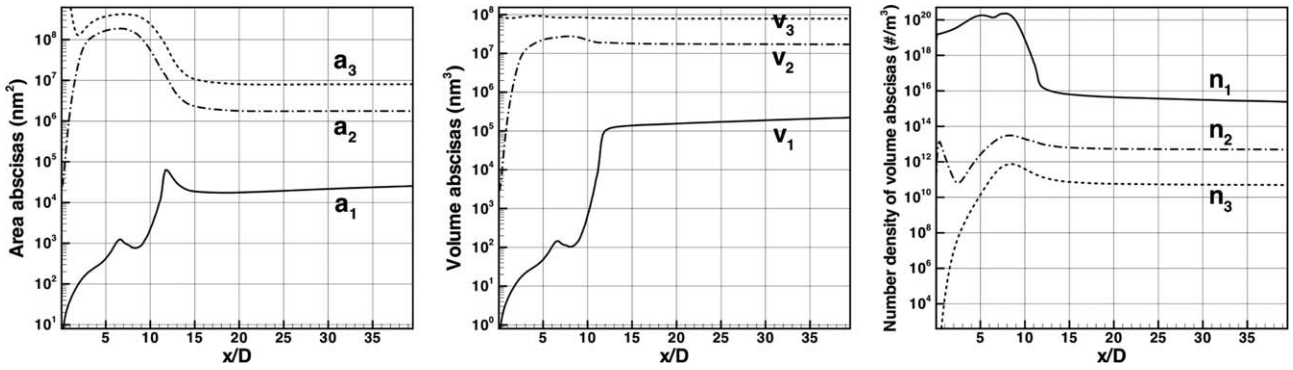

Figure 12. Time-averaged profiles of the (left) area and (middle) volume abscissas as well as (right) number density of three abscissa nodes of case A, along the centerline.

become larger. These results are consistent with the reduction in number density due to aggregation at the outer edge of the jet core. It is also seen that case A reaches its peak normalized volume concentration further upstream compared to case B.

Figure 15 also shows the surface area concentration normalized by the monomer surface area and filter-level surface density for both cases. Without surface growth, only sintering changes the conditional area node location in the CQMOM representation. However, sintering itself is strongly dependent on gas phase temperature and the size of the nanoparticles (see Fig. 1), thereby linking the area moment evolution to the volume moments and the gas phase composition. Indirectly, aggregation also plays an important role in sintering since the time scale for sintering (Eq. 28) is determined by the particle diameter. This interaction is important since aggregation and sintering have opposing effects on the total surface area concentration. Consequently, even in the presence of sintering, the local surface area concentration could increase due to dominant aggregation process (Fig. 14). This trend is seen in Figure 15, where a significant increase in surface area concentration is observed in the near-field. This is due to the dominant effect of aggregation with sintering effect not yet comparable to that of aggregation. However, after this point, the total surface area concentration suddenly decreases due to persistent sintering processes. Similarly, after x/D = 18, area concentration slowly increases because once again, aggregation rate is higher than sintering in the downstream.

Specific surface area (SSA) from experiments and simulations

The SSA is a quantitative measure of primary particle size. In CQMOM presentation, the SSA is modeled as

$$\mathrm{SSA} = \frac{m_{01}}{\rho_{\mathrm{TiO_2}} m_{10}}, \tag{43}$$

where $\rho_{\mathrm{TiO_2}}$ is the bulk density of solid TiO_2. In the experiment, particles are collected at x/D = 30 using a filter and used to obtain the SSA of the particulate population. To emulate this process, radially and azimuthally averaged SSA and primary particle size are computed from the simulations. Table 3 shows the comparison between simulations and experiments. In the simulations, case B shows larger primary particle size and lower SSA than case A. As discussed above, this is due to the longer flame length in case B.

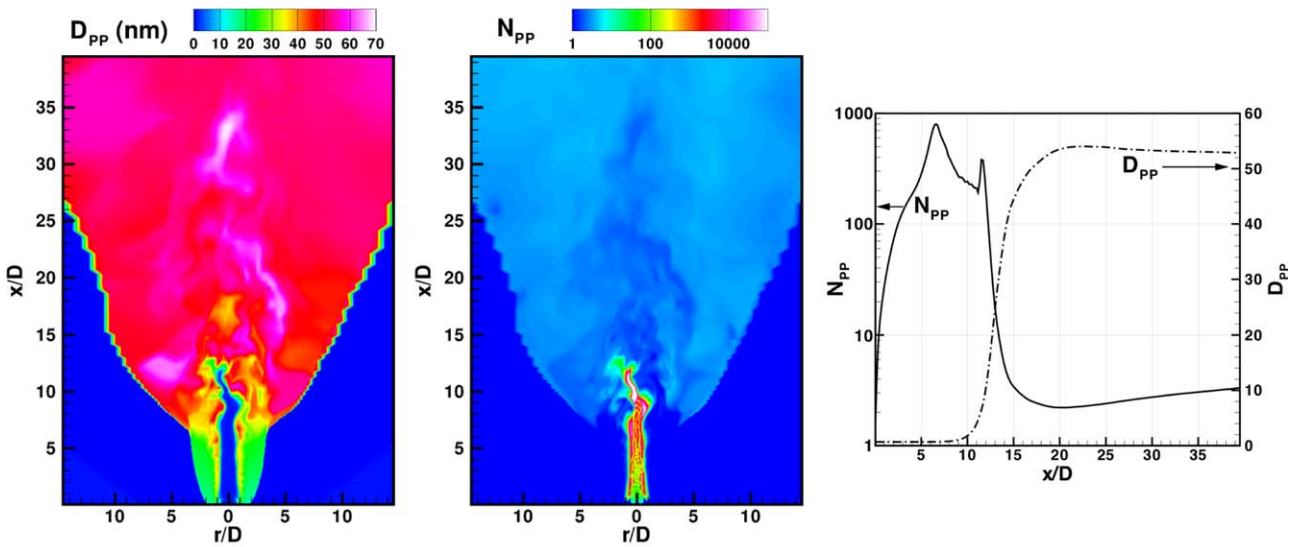

Figure 13. Instantaneous contour plots of the average (left) size and (middle) number of primary particles for case A.

Time-averaged N_{PP} (solid line) and D_{PP} (dash-dot) profiles along the centerline are provided on the right. [Color figure can be viewed in the online issue, which is available at wileyonlinelibrary.com.]

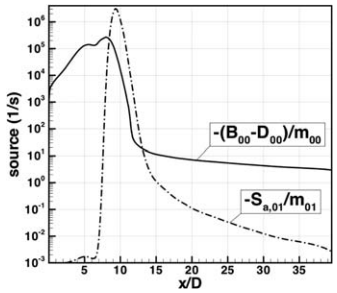

Figure 14. Time-averaged aggregation (solid line) and sintering (dash-dot line) source terms along the centerline.

With the sintering process considered, the CQMOM-based bivariate model exhibits significantly improved prediction for the SSA over the QMOM-based univariate model.[15] For example in the case B, SSA is improved vastly from 129 m^2/g[16] to 21.5 m^2/g here, which is reasonably close to that found in the experiment (15 m^2/g). The use of both a sintering model and a bivariate description leads to this improvement. It should also be noted that in the CQMOM approach, the particle surface area can be directly obtained from the bivariate formulation, while in the QMOM approach, this information has to be inferred from the volume nodes. The assumptions used therein could also contribute to errors in the QMOM-based surface area reported here. However, the primary particle size is considerably underpredicted by the bivariate model. These differences could be related to the differences in the flame length or the level of turbulence at the inflow. Without additional experimental data, it is not possible to determine the source of this discrepancy.

Conclusions

In this study, the LES-CQMOM approach for modeling flame synthesis in high-temperature flames was developed. This new approach accounts for the volumetric growth through aggregation and surface changes through sintering, in addition to incorporation detailed kinetic models for gas phase combustion and precursor oxidation. The nanoparticle NDF was described using the CQMOM approach with three volume nodes and one area node for each of the volume nodes. The stiffness in the sintering source terms were handled using a fractional time-stepping procedure along with semi-implicit ODE solvers. This LES-CQMOM framework provides a comprehensive mathematical formulation for handling particulate evolution in such hydrocarbon-based flames.

Table 3. Comparison of LES Results of Primary Particle Diameter and SSA Against the Experimental Data[29]

		LES	Experiment
Primary particle diameter (nm)	Case A	53.3	(not reported)
	Case B	66.0	100 ~105
SSA (m^2/g)	Case A	26.6	~15
	Case B	21.5	~15

The LES-CQMOM approach was then used to simulate flame synthesis in a methane-air flame with titanium tetrachloride as the precursor. Simulation results indicate that precursor oxidation occurs on the rich side of the fuel jet, leading to very high particle number density in this region. The effect of aggregation is dominant in this region, causing the number density to decrease as the particles move away through convection. Simultaneously, the surface area was found to increase. Further downstream, the average temperature in the flow is around 1200 K, where sintering rates are sufficiently high and cause a drastic reduction in the surface area of the particles. Overall, it appears that the different particle evolution processes are spatially separated. The use of the low-speed air stream causes the flame to be longer, and the nanoparticles have to travel further downstream before reaching the maximum volume concentration. These features indicate that the nanoparticle evolution could be precisely controlled by altering the flow rates of the streams. Comparisons with experimental data show that the LES-CQMOM approach overpredicts SSA while underpredicting primary particle size. This is attributed to the discrepancy

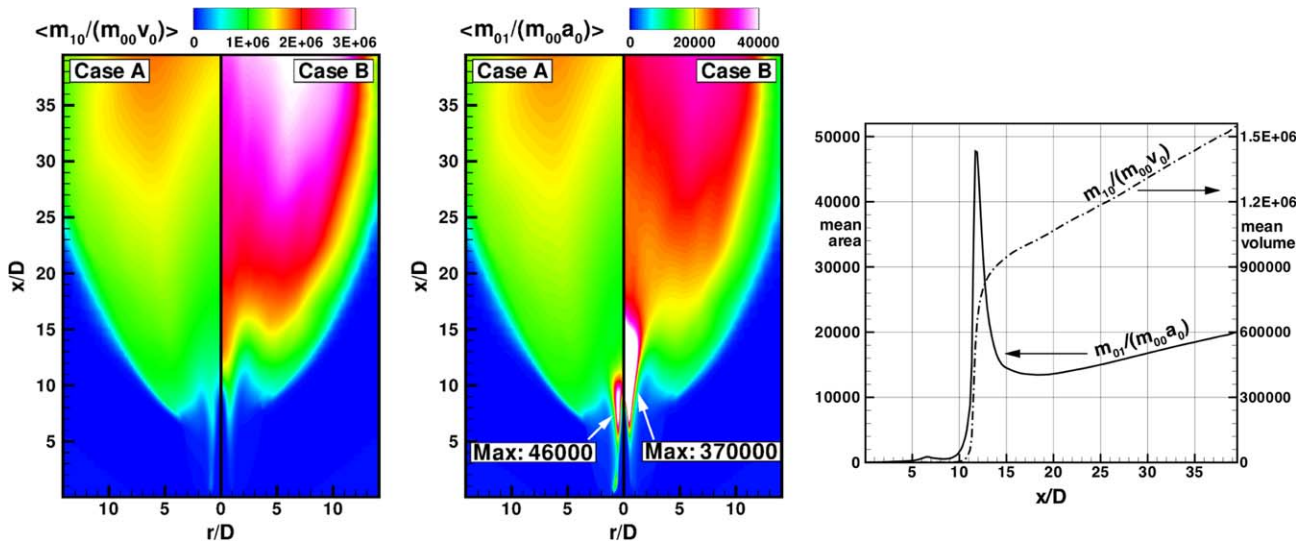

Figure 15. Mean normalized particle (left) volume and (middle) surface area for both cases A and B.

The nucleus volume and surface area are $v_0=0.166\text{nm}^3$ and $a_0=1.46\text{nm}^2$, respectively, leading to a diameter of 0.682nm. Centerline profiles of case A are provided on the right. [Color figure can be viewed in the online issue, which is available at wileyonlinelibrary.com.]

found in the flame length and the lack of appropriate inflow conditions from the experimental study. It is inferred that the experimental jet is far less turbulent than simulated jet, which will lead to a longer flame. More detailed experimental data will significantly aid validation.

Acknowledgments

This work was supported by a grant from the National Science Foundation (CBET-0730369). The authors would like to thank Prof. Sotiris E. Pratsinis (ETH, Zurich) for sharing details of the experiments and for providing valuable feedback. The simulations were carried out at the Texas Advanced Computer Center (TACC) on the Ranger supercomputer. The authors thank TACC for providing compute time on Ranger.

Literature Cited

1. Pratsinis SE. Aerosol-based technologies in nanoscale manufacturing: from functional materials to devices through core chemical engineering. *AIChE J*. 2010;56(12):3028–3035.
2. Strobel R, Pratsinis SE. Flame aerosol synthesis of smart nanostructured materials. *J Mater Chem.* 2007;17:4743–4756.
3. Johannessen T, Pratsinis SE, Livbjerg H. Computational fluid-particle dynamics for the flame synthesis of alumina particles. *Chem Eng Sci*. 2000;55:177–191.
4. Johannessen T, Pratsinis SE, Livbjerg H. Computational analysis of coagulation and coalescence in the flame synthesis of titania particles. *Powder Technol.* 2001;118(3):242–250.
5. Yu M, Lin J, Chan T. Numerical simulation of nanoparticle synthesis in diffusion flame reactor. *Powder Technol.* 2008;181:9–20.
6. Akroyd J, Smith AJ, Shirley R, McGlashan L, Kraft M. A coupled CFD-population balance approach for nanoparticle synthesis in turbulent reacting flows. *Cheml Eng Sci*. 2011;66:3792–3805.
7. Wang G, Garrick S. Modeling and simulation of titania synthesis in two-dimensional methane-air flames. *J Nanopart Res.* 2005;7:621–632.
8. Kempf A, Lindstedt RP, Janicka J. Large-eddy simulation of bluff-body stabilized nonpremixed flame. *Combust Flame.* 2006;144(1-2):170–189.
9. Pitsch H. Large-eddy simulation of turbulent combustion. *Annu Rev Fluid Mech.* 2006;38:453–482.
10. Raman V, Pitsch H. Large-Eddy simulation of bluff-body stabilized non-premixed flame using a recursive-refinement procedure. *Combust Flame*. 2005;142(4):329–347.
11. Raman V, Pitsch H, Fox RO. A consistent hybrid LES-FDF scheme for the simulation of turbulent reactive flows. *Combust Flame*. 2005;143(1-2):56–78.
12. West RH, Shirley RA, Kraft M. A detailed kinetic model for combustion synthesis of titania from $TiCl_4$. *Combust Flame*. 2009;156(9):1764–1770.
13. Mehta M, Raman V, Fox RO. On the role of gas-phase and surface chemistry in the production of titania nanoparticles in turbulent flames. *Chemical Engineering Science* 2012;104:1003–1018.
14. Kim HJ, Jeong JI, Park Y, Yoon Y, Choi M. Modeling of generation and growth of non-spherical nanoparticles in a co-flow Flame. *J Nanopart Res.* 2003;5:237–246. Available at: http://dx.doi.org/10.1023/A:1025570125689.
15. Sung Y, Raman V, Fox RO. Large eddy simulation based multiscale modeling of TiO_2 nanoparticle synthesis in a turbulent flame reactor using detailed nucleation chemistry. *Chem Eng Sci.* 2011;66(19):4370–4381.
16. Mehta M, Sung Y, Raman V, Fox RO. Multiscale modeling of TiO2 nanoparticle production in flame reactors: effect of chemical mechanism. *Ind Eng Chem Res.* 2010;49(21):10663–10673.
17. Yuan C, Fox RO. Conditional quadrature method of moments for kinetic equations. *J Comput Phys.* 2011;230:8216–8246.
18. Germano M. Turbulence: the filtering approach. *J Fluid Mech.* 1992;238:325–336.
19. Smagorinsky J. General circulation experiments with the primitive equations - I. *The basic experiment. Mon Weather Rev*. 1963;91:99–164.
20. Ghosal S, Lund TS, Moin P, Akselvoll K. A dynamic localization model for large-eddy simulation of turbulent flows. *J Fluid Mech.* 1995;286:229–255.
21. Moin P, Squires K, Cabot W, Lee S. A dynamic subgrid-scale model for compressible turbulence and scalar transport. *Phys Fluids A.* 1991;3:2746–2757.
22. Bowman CT, Hanson RK, Davidson DF, et al. Gri-Mech 2.11. Available at: http://www.me.berkeley.edu/gri_mech/. 1995.
23. Peters N. *Turbulent Combustion*. Cambridge University Press, 2000.
24. Jimenez J, Linan A, Rogers MM, Higuera FJ. A priori testing of subgrid models for chemically reacting non-premixed turbulent flows. *J Fluid Mech.* 1997;349:149–171.
25. Pitsch H, Steiner H. Large-eddy simulation of a turbulent piloted methane/air diffusion flame (Sandia Flame D). *Phys Fluids*. 2000;12(10):2541–2554.
26. Pierce CD, Moin P. A dynamic model for subgrid-scale variance and dissipation rate of a conserved scalar. *Phys Fluids.* 1998;10:3041–3044.
27. Pierce CD, Moin P. Progress-variable approach for large-eddy simulation of non-premixed turbulent combustion. *J Fluid Mech.* 2004;504:73–97.
28. Pitsch H. A C++ computer program for 0-D and 1-D laminar flame calculations, RWTH: Aachen, 1998.
29. Pratsinis SE, Zhu W, Vemury S. The role of gas mixing in flame synthesis of titania powders. *Powder Technol*. 1996;86(1):87–93.
30. Fuchs NA. The Mechanics of Aerosols. New York: Pergamon Press, 1964.
31. Marchisio DL, Fox RO. Computational Models for Polydisperse Particulate and Multiphase Systems. New York: Cambridge University Press, 2013.
32. Friedlander SK, Wu MK. Linear rate law for the decay of excess surface area of a coalescencing solid particle. *Phys Rev B*. 1994;49:347.
33. Yu M, Lin J, Chan T. Effect of precursor loading on non-spherical TiO_2 nanoparticle synthesis in a diffusion flame reactor. *Chem Eng Sci*. 2008;63:2317–2329.
34. Fox RO. *Computational Models for Turbulent Reacting Flows*. Cambridge University Press, 2003:419.
35. Cheng J, Fox RO. Kinetic modeling of nanoprecipitation using CFD coupled with a population balance. *Ind Eng Chem Res*. 2010;49(21):10651–10662.
36. McGraw R. Description of aerosol dynamics by the quadrature method of moments. *Aerosol Sci Tech.* 1997;27:255–265.
37. Desjardins O, Blanquart G, Balarac G, Pitsch H. High order conservative finite difference scheme for variable density low Mach number turbulent flows. *J Comput Phys*. 2008;227:7125–7159.
38. Liu XD, Osher S, Chan T. Weighted essentially non-oscillatory schemes. *J Comput Phys.* 1994;115;200–212.

Manuscript received July 16, 2012, and revision received Oct. 3, 2013.